Heat transfer and force balance approaches in bubble dynamic study during subcooled flow boiling of water–ethanol mixture

B. G. Suhas & A. Sathyabhama

Taylor & Francis
Taylor & Francis Group

Check for updates

Heat transfer and force balance approaches in bubble dynamic study during subcooled flow boiling of water–ethanol mixture

B. G. Suhas and A. Sathyabhama

Mechanical Engineering Department, National Institute of Technology, Srinivasanagara, Surathkal, Mangalore, Karnataka, India

ABSTRACT

In this paper, the subcooled flow boiling heat transfer coefficient of pure water, water–ethanol mixture and pure ethanol is determined experimentally in horizontal rectangular channels for various parameters like heat flux, mass flux and channel inlet temperatures. Flow visualization is carried out using high speed camera. The bubble departure diameter, growth period and waiting period of bubbles are determined. Correlations are developed for subcooled flow boiling Nusselt number of water–ethanol mixture based on force balance approach and heat transfer approach. The parameters considered for correlation are grouped as dimensionless numbers by Buckingham π-theorem. The significance of each dimensionless number on heat transfer coefficient is discussed. The correlations developed for subcooled flow boiling heat transfer coefficient are validated with the experimental data. They are found to be in good agreement with the experimental data. It is found that the correlation based on force balance approach predicts the subcooled flow boiling Nusselt number well when compared with that of heat transfer approach correlation.

Introduction

Flow boiling of binary mixture is applicable in chemical, refrigeration, air-conditioning and air separation industries [1–3]. Exact value of heat transfer coefficient of the fluid in these applications can be determined by conducting experiments. Since the experiments are expensive and tedious, correlations can be used as an alternate method to predict heat transfer coefficient. Two types of correlations are empirical correlation and mechanism-based correlation [4]. The empirical correlation is obtained by plotting the curves which give an explicit relation between several parameters [5]. The mechanism-based correlation or mechanistic model incorporates thermo physical properties, thermodynamic properties and physics involved in the boiling phenomena [6]. During last five decades, models have been developed to predict the heat transfer rate during the flow boiling. These models can be broadly classified into three categories: i) empirical correlations for wall heat flux, ii) empirical correlations for partitioning of wall heat flux, and iii) mechanistic models for wall heat flux partitioning. The empirical correlations for wall heat flux are generally limited to the prediction of total wall heat flux for a particular flow situation. They are merely correlations of experimental data and as such do not include modeling of the heat transfer mechanisms involved [7]. The correlation to predict the heat flux in the nucleate boiling region for water and ethanol was developed based on the experimental data obtained for cylindrical tube between 5 and 7 mm. It was found that the correlation predicts the experimental value with a maximum deviation of ±16%. The already existing Rohsenow correlation was modified to predict the heat flux in the nucleate boiling by introducing

---

CONTACT B. G. Suhas ✉ suhas_bg@yahoo.co.in 🖃 Mechanical Engineering Department, National Institute of Technology, Srinivasanagara, Surathkal, Mangalore 575025, Karnataka, India.

Color versions of one or more of the figures in the article can be found online at www.tandfonline.com/ueht.

Table 1. Experimental parameters.

Parameter	Range
Ethanol volume fraction	0, 0.25, 0.5, 0.75, 1
Heat Flux	90.4 to 133.47 (kW/m^2)
Mass Flux	76.67 to 228.33 (kg/m^2-s)
Channel inlet temperature	303 to 323 (K)

various π parameters [8].Saturated boiling heat transfer coefficient correlation was developed for water and ethylene glycol in vertical tubes. The mean deviation between the calculated and the measured boiling heat transfer coefficient was 21.4% [9]. The correlations are available for saturated boiling of mixtures. But only few correlations are available for subcooled flow boiling region of mixtures. Subcooled boiling heat transfer coefficient correlation was developed by different sets of dimensionless number for water, hydrocarbons, cryogenic fluids and refrigerants which compared well with the experimental data [10].

Liaofei Yin et al [11] carried out the force balance in the subcooled flow boiling region. It is assumed that the bubble detaches from the surface when the buoyancy and drag forces are able to overcome the force due to surface tension. The drag force includes the quasi-steady drag force, the unsteady drag due to asymmetric growth of the bubble and the shear lift force. The liquid drag on the bubble due to asymmetrical bubble growth acting in the direction opposite to liquid flow is important in holding the bubble to its nucleation site before departure. The literature review presented above is related to pure component. The bubble dynamics and force balance analysis are not available in plenty for mixture subcooled boiling.

The present work is aimed at developing correlation for subcooled flow boiling Nusselt number of water–ethanol mixture. The water ethanol mixture can be used in cooling of HEV battery module when powered by battery and the same mixture can also be used for fumigation process when powered by fuel. The heat generation rate for these batteries during charging is at an average of 20 W per cell and may peak up to 50 W per cell [12]. This increases the temperature of the battery cells approximately to 70 to 80° C. Higher temperature of the batteries will lead to chemical breakdown and eventually leads to malfunction. Hence, the cooling of the battery module is necessary [13]. The cold plate which acts as a conductive member is placed above the battery module and fluid is passed through this plate. The liquid undergoes subcooled boiling when it passes through the cold plate. Therefore, to design the cold plate, knowledge of heat transfer coefficient of this mixture is essential. The experiment is conducted to find the subcooled flow boiling heat transfer coefficient of water–ethanol mixture for various parameters such as heat fluxes mass fluxes, inlet temperatures and volume fractions of ethanol. Table 1 shows the experimental parameters and their range. At 90.4 kW/m^2, the subcooled boiling takes place for both water and ethanol. If the heat flux is lower than 90.4 kW/m^2, subcooled boiling of water will not commence, instead it will be in forced convective region. If the heat flux is higher than 90.4 kW/m^2, saturated boiling of ethanol will be initiated. Bubble departure diameter is measured through visualization by high speed camera. The new correlation based on force balance approach is developed by grouping the bubble departure diameter, bubble growth period, waiting period into dimensionless numbers. The accuracy of this correlation is tested by comparing with the experimental data and with the correlation which is developed by heat transfer approach.

Methodology

Experimental setup and procedure

The schematic diagram of experimental test set up is shown in Figure 1. The experimental test set up is a closed loop having a rectangular aluminum block consisting of two rectangular channels, condenser coil dipped in ice water bath, reservoir, preheater and pump having variable flow rate.
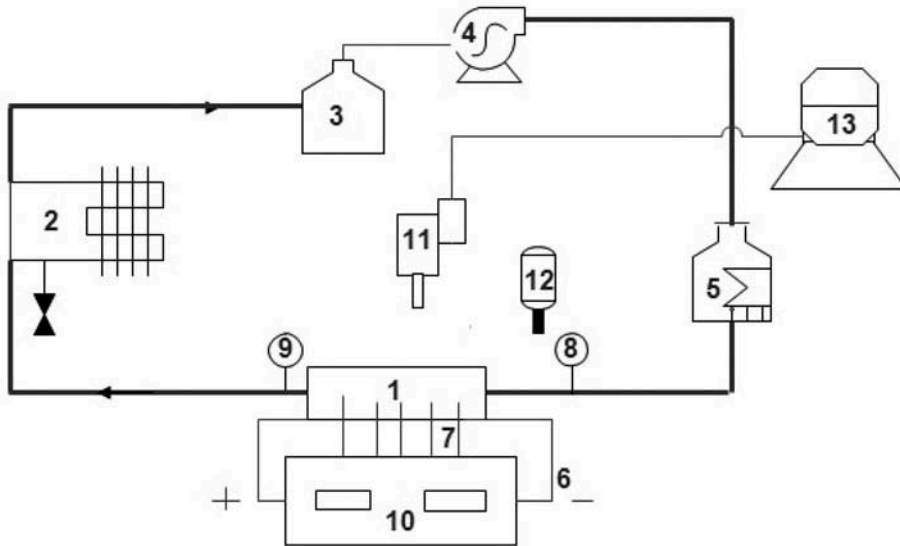
Figure 1. Schematic diagram of experimental setup. (1) Rectangular aluminum block consisting of two rectangular channels. (2) Condenser coil dipped in ice water bath. (3) Reservoir. (4) Pump having variable flow rate. (5) Preheater. (6) Cartridge heaters. (7) Thermocouples to measure wall temperature. (8) Thermocouple to measure channel inlet temperature (9) Thermocouple to measure channel outlet temperature. (10) Temperature indicator panel (11) High speed camera. (12) Light source.(13) Data Aquisition system for flow visualization.

Figure 2. Aluminum block with rectangular channels.

The aluminum block consisting of two channels of 10 mm (width) × 10 mm (height) × 150 mm (Length) is shown in Figure 2. The two cartridge heaters are inserted inside the aluminum block. Heat loss is prevented by providing mineral wool as insulating material. The wall temperatures, the fluid inlet and outlet temperatures of the channel are measured by thermocouples. The temperature reading is obtained in the temperature indicator panel. The high speed camera is used for flow visualization. Table 2 shows the equipments used in the present experiment. Figure 3 shows the thermocouples arrangement in the cold plate to measure wall temperature and to calculate heat flux. The first set of five thermocouples (T_{11}, T_{12}, T_{13}, T_{14} and T_{15}) is placed 2 mm below the channel in a row. The second set of five thermocouples (T_{21}, T_{22}, T_{23}, T_{24} and T_{25}) is placed 20 mm below the first row of thermocouples. The distance between two thermocouples in a row is 25 mm. Two cylindrical cartridge heaters are placed 40 mm below the channels. Due to the possibility of solubility

Table 2. Equipments used in the present experiment.

Equipments	Specifications
k-type thermocouples for wall temperature measurements (12 no's)	Range: −20°C to 400°C, Sheath length: 20 mm, sheath diameter: 1.2 mm
Cartridge heater (2 no's)	Diameter: 12.7 mm, Length: 180 mm, capacity: 750 W
Peristaltic pump	Capacity: 100 liters per hour, Operating pressure: Atmospheric
Preheater	Chamber capacity: 4 Liters, Heater capacity: 3 kW.
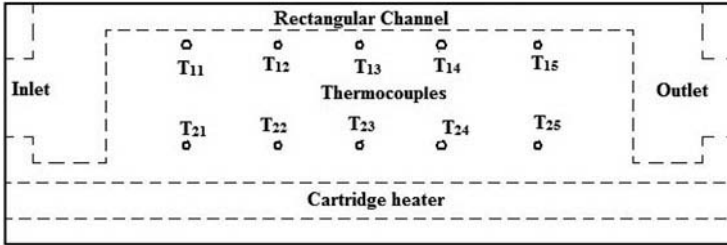
Figure 3. Arrangement of thermocouples in the cold plate.

of air in water and ethanol, degassing is done for about thirty minutes before commencing the experiment. The liquid is preheated and pumped through the test set up. The heat is supplied to the channel to boil the liquid. The liquid after getting cooled in the condenser coil enters the reservoir. The experiment is conducted after the degassing procedure [14].

Flow visualization is carried out using high speed camera to understand the phenomena of heat transfer during the subcooled flow boiling of the mixture. The LED PAR light is used as light source. The specifications of high speed camera and LED light are given in Table 3. The block diagram in Figure 4 gives the steps which are followed to measure the bubble departure diameter and contact angle by an image processing tool in Lab view vision builder software. A tangent is drawn along the bubble as shown in Figure 5(a). The intersection of the tangent and the channel surface is considered as contact angle. The channel width is considered as the reference length to measure the departure diameter. The camera is placed at the top of the channel as shown in Figure 5(b). The trigonometric relations are considered to calculate the actual contact angle. However, there is no significant variation in measuring the bubble departure diameters because the bubbles are assumed to be spherical in shape.

From the trigonometric relation:

$$\frac{AB}{BC} = \tan(A^\circ)$$

AB is the distance from the camera lens to the point on the camera stand which is parallel to the bottom wall of channel. BC is the distance from the bottom wall of the channel to the point on the camera stand which is parallel to the bottom wall of channel.

Table 3. Specifications of high speed camera and source light.

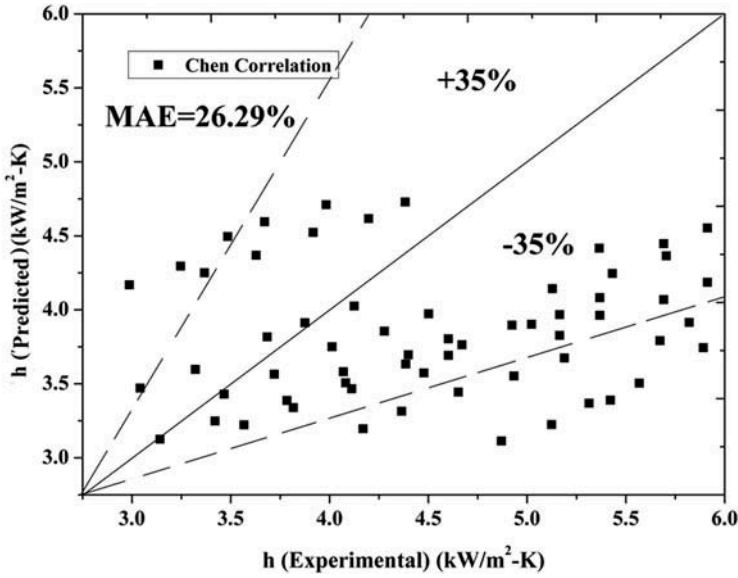| Processor	AOS Promon 501
Lens	50 mm
Aperture setting	f/1.4 D
Shutter speed	1/15
Frames per second	1459
Resolution	480 × 240 pixels
LED PAR Light	Slim die cast body, Power 120W, beam 25 degree, CRI>85, DMX 512 Auto, sound active, 3 section light weight aluminum stand
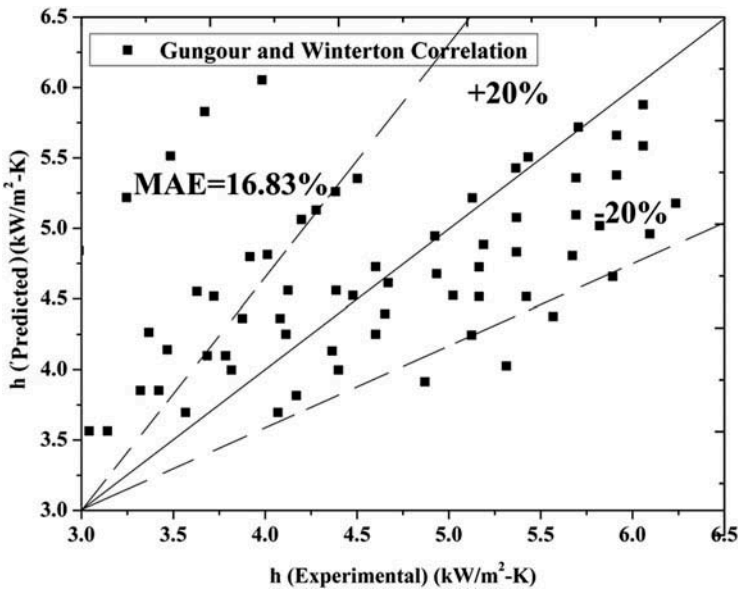
Data reduction

Bottom wall temperature of the channel is calculated by temperature gradient between the first row and second row of thermocouples in aluminum block. Fourier's law of heat conduction is applied to calculate the heat flux from the measured values of temperature gradient and known value of thermal conductivity.

$$q'' = -k\frac{dT}{dx} \tag{1}$$

The heat flux is calculated by substituting the values of thermal conductivity of aluminum, temperature gradient in Eq. (1) as shown by Eq. (2).

$$q'' = -k\frac{(T_{sr} - T_{fr})}{(X_{sr} - X_{fr})} \tag{2}$$

The heat flux is assumed to be the same for the bottom wall of the channel as the first row, since it is very near to the first rows of thermocouples (i.e., 2 mm). The wall temperature is calculated by Eq. (3).

$$T_W = \frac{-q''}{k}(X_w - X_{fr}) + T_{fr} \tag{3}$$

The heat transfer coefficient is calculated by Eq. (4) from the calculated values of heat flux, calculated values of wall temperature and measured values of outlet temperature. The average of five readings of wall temperature is considered to determine the difference between the wall and fluid temperature. Fluid temperature is the average fluid temperature of the channel inlet and the outlet.

$$h = \frac{q''}{(T_w - T_f)} \tag{4}$$

It is observed that the heat flux value is higher at the inlet of the channel and decreases along length of the channel. It is also observed that the wall temperature is lower at the entrance and marginally increases along the channel length. Therefore, the average of five heat fluxes and wall temperatures which are obtained from five different points along the length of the channel is considered to calculate the heat transfer coefficient.

Uncertainties

According to International Bureau of weights and measures (IBWM) and International organization of standards, (ISO) random independent variables may be calculated using root-sum-square (RSS) of standard deviation [15].

$$\omega_{ip} = \sqrt{\omega_{iresolution}^2 + \omega_{iconversion}^2 + \omega_{icalibration}^2 + s_{2\sigma_i}^2} \tag{5}$$

After determining the uncertainty of independent variables, the uncertainties of calculated parameters are determined by McClintock and Kline method [16].

$$\omega_{cp}^2 = \sum_{i=1}^{n}\left(\frac{\partial f}{\partial x_i}\right)^2 \omega_{x_i}^2 \tag{6}$$

Table 4 shows the uncertainties of independent and measured parameters.

Table 4. Uncertainties of measured and calculated parameters.

Parameters	Uncertainties
Thermocouple	$\pm 0.35°C$ (RSS)/ $\pm 0.1°C$ (resolution)
Preheater temperature	$\pm 0.1°C$ (resolution)
Mass flow rate	$\pm 2.32\%$
Mass flux	$\pm 0.77\%$
Heat flux	$\pm 13.3\%$
Heat transfer coefficient	$\pm 9.11\%$
Bubble departure diameter	$\pm 13.02\%$

Results and discussions

The effect of ethanol volume fraction addition on subcooled flow boiling heat transfer coefficient is discussed. The correlation based on force balance approach is also developed and is compared with the heat transfer approach. Table 5 provides the data source which include the range of parameters covered.

Table 5. Data source of the present experiment.

Data points	Ethanol volume fraction (%)	q'' (W/m^2)	G (kg/m^2-s)	T_{in} (K)	d_{dep} (mm)	t_{gp} (ms)	t_{wp} (ms)
1	0	90400	76.67	303	0.583	16.12	18.34
2	0	90400	115.33	303	0.551	15.33	16.44
3	0	90400	151.33	303	0.532	14.78	17.24
4	0	90400	191.67	303	0.514	13.45	15.45
5	0	90400	228.33	303	0.491	12.45	16.45
6	0	90400	76.67	313	0.704	21.24	23.88
7	0	90400	115.33	313	0.683	19.67	22.68
8	0	90400	151.33	313	0.664	18.76	21.76
9	0	90400	191.67	313	0.647	16.96	20.63
10	0	90400	228.33	313	0.622	15.44	19.32
11	0	90400	76.67	323	0.783	24.36	28.41
12	0	90400	115.33	323	0.761	23.22	27.33
13	0	90400	151.33	323	0.745	22.33	26.14
14	0	90400	191.67	323	0.723	21.78	25.24
15	0	90400	228.33	323	0.706	21.45	24.19
16	25	90400	76.67	303	0.561	13.65	15.87
17	25	90400	115.33	303	0.529	12.88	13.97
18	25	90400	151.33	303	0.51	12.33	14.77
19	25	90400	191.67	303	0.492	10.96	12.98
20	25	90400	228.33	303	0.469	10.03	13.98
21	25	90400	76.67	313	0.686	18.69	21.41
22	25	90400	115.33	313	0.665	17.14	20.21
23	25	90400	151.33	313	0.646	16.22	19.29
24	25	90400	191.67	313	0.629	14.41	18.16
25	25	90400	228.33	313	0.604	12.89	16.85
26	25	90400	76.67	323	0.766	23.01	25.94
27	25	90400	115.33	323	0.744	21.87	24.86
28	25	90400	151.33	323	0.728	20.98	23.67
29	25	90400	191.67	323	0.706	20.43	22.77
30	25	90400	228.33	323	0.689	20.1	21.72
31	50	90400	76.67	303	0.593	15.99	13.4
32	50	90400	115.33	303	0.561	15.21	11.5
33	50	90400	151.33	303	0.542	14.67	12.3
34	50	90400	191.67	303	0.524	13.3	10.51
35	50	90400	228.33	303	0.501	12.28	11.51
36	50	90400	76.67	313	0.716	21.14	18.94
37	50	90400	115.33	313	0.695	19.48	17.74
38	50	90400	151.33	313	0.676	18.74	16.82
39	50	90400	191.67	313	0.659	16.88	15.69
40	50	90400	228.33	313	0.634	15.27	14.38
41	50	90400	76.67	323	0.798	25.66	23.47
42	50	90400	115.33	323	0.776	24.53	22.39

Table 5. (Continued).

Data points	Ethanol volume fraction (%)	q'' (W/m^2)	G (kg/m^2-s)	T_{in} (K)	d_{dep} (mm)	t_{gp} (ms)	t_{wp} (ms)
43	50	90400	151.33	323	0.760	23.7	21.2
44	50	90400	191.67	323	0.738	23.01	20.3
45	50	90400	228.33	323	0.724	22.72	19.25
46	75	90400	76.67	303	0.608	18.17	10.93
47	75	90400	115.33	303	0.576	17.49	9.03
48	75	90400	151.33	303	0.557	17.03	9.83
49	75	90400	191.67	303	0.539	15.71	8.04
50	75	90400	228.33	303	0.5164	14.51	9.04
51	75	90400	76.67	313	0.732	23.41	16.47
52	75	90400	115.33	313	0.711	21.96	15.27
53	75	90400	151.33	313	0.692	21.02	14.35
54	75	90400	191.67	313	0.675	19.29	13.22
55	75	90400	228.33	313	0.65	17.45	11.91
56	75	90400	76.67	323	0.813	28.14	21
57	75	90400	115.33	323	0.791	27.23	19.92
58	75	90400	151.33	323	0.775	26.35	18.73
59	75	90400	191.67	323	0.758	25.46	17.83
60	75	90400	228.33	323	0.736	25.29	16.78
61	100	90400	228.33	323	0.609	16.89	8.46
62	100	90400	228.33	323	0.568	16.31	6.56
63	100	90400	228.33	323	0.549	15.65	7.36
64	100	90400	228.33	323	0.531	14.53	5.57
65	100	90400	228.33	323	0.508	13.23	6.57
66	100	90400	228.33	323	0.724	22.13	14
67	100	90400	228.33	323	0.703	20.68	12.8
68	100	90400	228.33	323	0.684	19.74	11.88
69	100	90400	228.33	323	0.667	18.14	10.75
70	100	90400	228.33	323	0.642	16.31	9.44
71	100	90400	228.33	323	0.803	26.98	18.53
72	100	90400	228.33	323	0.784	25.99	17.45
73	100	90400	228.33	323	0.768	25.07	16.26
74	100	90400	228.33	323	0.746	24.31	15.36
75	100	90400	228.33	323	0.729	24.14	14.31
76	0	109610	76.67	303	0.462	11.26	15.46
77	0	109610	115.33	303	0.442	10.24	14.28
78	0	109610	151.33	303	0.432	9.38	13.66
79	0	109610	191.67	303	0.412	7.67	11.63
80	0	109610	228.33	303	0.392	8.76	12.78
81	0	133470	76.67	303	0.392	6.48	12.06
82	0	133470	115.33	303	0.362	5.78	11.49
83	0	133470	151.33	303	0.342	5.23	10.24
84	0	133470	191.67	303	0.322	3.28	8.26
85	0	133470	228.33	303	0.302	4.78	9.19
86	0	109610	76.67	313	0.562	15.24	18.33
87	0	109610	115.33	313	0.542	14.38	17.68
88	0	109610	151.33	313	0.512	13.08	16.29
89	0	109610	191.67	313	0.492	12.47	15.48
90	0	109610	228.33	313	0.472	11.78	14.77
91	0	133470	76.67	313	0.482	10.89	15.68
92	0	133470	115.33	313	0.462	10.35	14.29
93	0	133470	151.33	313	0.442	9.88	13.56
94	0	133470	191.67	313	0.422	7.93	12.69
95	0	133470	228.33	313	0.402	6.24	11.42
96	0	109610	76.67	323	0.692	20.46	22.45
97	0	109610	115.33	323	0.672	19.21	21.35
98	0	109610	151.67	323	0.652	17.98	20.14
99	0	109610	191.67	323	0.632	15.87	18.63
100	0	109610	228.33	323	0.612	14.96	17.89
101	0	133470	76.67	323	0.592	16.78	18.25
102	0	133470	115.33	323	0.572	15.38	17.64
103	0	133470	151.67	323	0.542	14.24	16.24
104	0	133470	191.67	323	0.522	13.69	15.48
105	0	133470	228.33	323	0.502	12.89	13.93

(Continued)

Table 5. (Continued).

Data points	Ethanol volume fraction (%)	q″ (W/m²)	G (kg/m²-s)	T$_{in}$ (K)	d$_{dep}$ (mm)	t$_{gp}$ (ms)	t$_{wp}$ (ms)
106	25	109610	76.67	303	0.438	9.02	13.22
107	25	109610	115.33	303	0.421	8	12.04
108	25	109610	151.33	303	0.409	7.14	11.42
109	25	109610	191.67	303	0.39	5.43	9.39
110	25	109610	228.33	303	0.371	6.52	10.54
111	25	109610	76.67	313	0.368	4.24	9.82
112	25	109610	115.33	313	0.337	3.54	9.25
113	25	109610	151.33	313	0.32	2.99	8
114	25	109610	191.67	313	0.301	1.04	6.02
115	25	109610	228.33	313	0.282	2.54	6.95
116	25	109610	76.67	323	0.539	13	16.09
117	25	109610	115.33	323	0.516	12.14	15.44
118	25	109610	151.33	323	0.488	10.84	14.05
119	25	109610	191.67	323	0.469	10.23	13.24
120	25	109610	228.33	323	0.45	9.54	12.53
121	50	109610	76.67	303	0.473	8.65	13.44
122	50	109610	115.33	303	0.459	12.49	16.69
123	50	109610	151.33	303	0.443	11.47	15.51
124	50	109610	191.67	303	0.423	10.61	14.89
125	50	109610	228.33	303	0.412	8.9	12.86
126	50	109610	76.67	313	0.41	9.99	14.01
127	50	109610	115.33	313	0.369	7.71	13.29
128	50	109610	151.33	313	0.363	7.01	12.72
129	50	109610	191.67	313	0.338	6.46	11.47
130	50	109610	228.33	313	0.318	4.51	9.49
131	50	109610	76.67	323	0.573	6.01	10.42
132	50	109610	115.33	323	0.552	16.47	19.56
133	50	109610	151.33	323	0.522	15.61	18.91
134	50	109610	191.67	323	0.501	14.31	17.52
135	50	109610	228.33	323	0.481	13.7	16.71

Validation

The experimental values obtained for water at mass flux of 76.67 kg/m²-s, heat flux from 90.4 to 133.47 kW/m² and inlet temperature at 303 K are validated with available subcooled boiling literature correlations. Chen [17] redeveloped the Rohsenow correlation for subcooled boiling heat transfer coefficient:

$$h_{tp} = Fh_{fc} + Sh_{pb} \tag{7}$$

$$h_{fc} = 0.023 Re^{0.8} Pr^{0.4} \frac{k_l}{D_h} \tag{8}$$

$$h_{pb} = 0.00122 \frac{k^{0.79} C_P^{0.45} \rho_l^{0.49}}{\sigma^{0.5} \mu_l^{0.29} h_{fg}^{0.24} \rho_g^{0.24}} \Delta T_{Sat}^{0.24} \Delta p_{Sat}^{0.75} \tag{9}$$

$$F = \left(1 + \frac{1}{(\chi_{tt})^{0.5}} \right)^{1.78} \tag{10}$$

$$\chi_{tt} = \left(\frac{1-x}{x} \right)^{0.9} \left(\frac{\rho_g}{\rho_l} \right) \left(\frac{\mu_l}{\mu_g} \right)^{0.1} \tag{11}$$

$$S = \frac{1}{1 + 2.53 \times 10^{-6}Re^{1.17}} \tag{12}$$

The Reynolds number factor F and the suppression factor S were determined empirically from experimental data [18]. Figure 4 shows that 81.5% of present experimental data are predicted within $\pm 35\%$ error band, and 66.15% are predicted within error band of $\pm 20\%$. The MAE of experimental data while predicting using Chen correlation is 26.29%. The Chen correlation was developed by considering 600 data points for water and five organic fluids. The parameter range was vapor quality from 0.01 to 0.71, mass flux from 54 to 4070 kg/m^2-s, heat flux from 6.3 to 2397.5 kW/m^2, and saturation pressure from 0.055 to 3.48 MPa. The other reason for deviation is the presence of Reynolds number factor F in the Chen correlation. F is a function of Martinelli parameter (χ_{tt}) as shown in Eq. (10). Martinelli parameter is determined from vapor quality. Since the presence of vapor quality is negligible during the subcooled boiling, F is chosen as 1 in the present experiment.

Gungor and Winterton [10] modified the Chen correlation by introducing the dependence on the boiling number (Bo) in the enhancement factor E. They suggested Cooper correlation for pool boiling heat transfer component.

$$h_{pb} = 55\left(\frac{P}{P_{cr}}\right)^{0.12}\left[-log_{10}\left(\frac{P}{P_{cr}}\right)\right]^{-0.55}M^{-0.5}q''^{0.67} \tag{13}$$

$$S = \frac{1}{1 + 1.15 \times 10^{-6}E^2Re^{1.17}} \tag{14}$$

$$E = 1 + 24000Bo^{1.16} + 1.37\left(\frac{1}{\chi_{tt}}\right)^{0.86} \tag{15}$$

h_{tp} and h_{fc} are calculated by Eqs. (7) and (8), respectively. Figure 5 shows that 78.64% of present experimental data are predicted within $\pm 20\%$ error band, and 44.62% are predicted within error band of $\pm 10\%$. The MAE of experimental data while predicting with Gungour–Winterton correlation is 16.83%. The boiling number in Eq. (15) leads to relatively lower deviation when compared with that of Chen correlation. The Gungor and Winterton correlation was developed for 4300 data points for water, R11, R12, R113, R114 and Ethylene Glycol for various tube diameters, orientation of flow, mass flux, heat flux, saturation pressure and vapor quality. This is the reason for deviation of the present experimental data from those data predicted from the correlation.

Liu and Winterton [19] proposed a power-type addition model for the prediction of subcooled flow boiling heat transfer. The correlation for subcooled flow boiling heat transfer coefficient is expressed as:

$$h_{tp} = \sqrt{Fh_{fc}^2 + \left(Sh_{pb}\frac{T_{Wall} - T_{Sat}}{T_{Wall} - T_{Sat}}\right)^2} \tag{16}$$

$$S = \frac{1}{1 + 0.0055F^{0.1}Re_l^{0.16}} \tag{17}$$

h_{pb} is calculated by Eq. (5). Figure 6 shows that 69.23% of present experimental data are predicted within $\pm 20\%$ error band, and 38.46% are predicted within error band of $\pm 10\%$. The MAE of Liu and Winterton correlation while predicting the experimental data is 22.69%. The MAE of experimental data while predicting with Liu-Winterton correlation is 22.69%. Their experiments were carried out in tubes and annuli and covered a range of mass flux from 12.4 to 8180 kg/m^2-s, Pressure from 0.05 to 20 MPa, and T_{sub} from 0 to 173∘C.

Kandlikar [20] proposed subcooled boiling correlations for water and is given by Eq. (18):
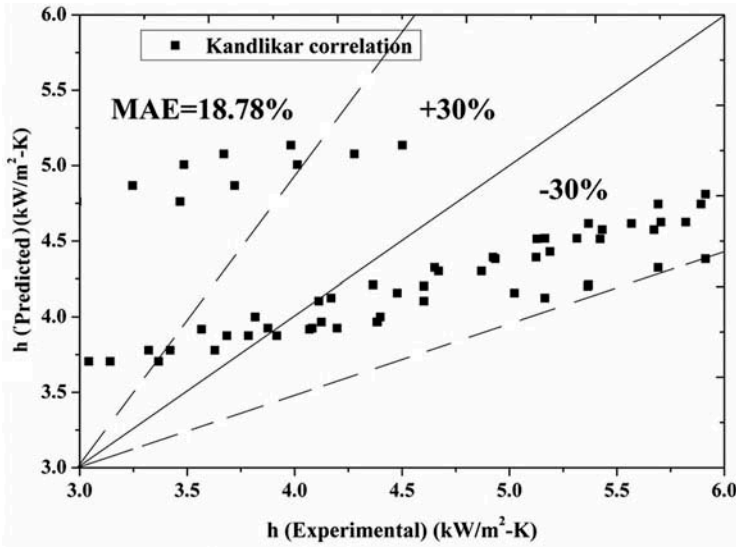

number plays vital role during subcooled flow boiling heat transfer and it also proved to be significant while predicting the subcooled flow boiling heat transfer coefficient by heat transfer approach [21]. Boiling number is defined as the ratio of heat flux to heat of evaporation. When heat flux increases, the active nucleation sites increase. Isolated bubbles are formed on active nucleation sites during nucleate boiling. After bubble inception, the superheated liquid layer which is pushed outward mixes with the subcooled liquid leading to agitation [22]. The heat flux is considered by combining the effect of transient conduction around nucleation sites and micro-layer evaporation below the bubbles. The departed bubble acts as an energy carrier by removing the heat from the channel wall surface. Hence, boiling number is more significant in the subcooled boiling region.

The deviation of the present experimental data from those predicted using correlations is also attributed to non-uniform temperature distribution in cold plate, assumption of one dimensional temperature distribution to calculate heat flux and impossibility of making the experimental system air tight.

Effect of ethanol volume fraction on heat transfer

The components in the liquid mixture have different evaporation rates. The lower boiling component escapes from the liquid–vapor interface and the higher boiling component accumulates near the liquid–vapor interface. The layer of the concentration gradient forms near the interface. Because of two phase and convective heat transfer, the concentration gradient layer exists not only at the surface of the bubble but also at the liquid–vapor interface at the bottom wall. Mass diffusion which exists during the convective heat transfer process affects the heat transfer coefficient of mixture during the subcooled flow boiling process. The lower boiling component in the liquid bulk has to pass through the diffusion layer before arriving at the interface. Therefore, for a mixture, the heat transfer coefficients are affected not only by the interaction between the two phase flow and the convective heat transfer, but also by the mass transfer resistance inside the diffusion layer [23]. The concentration gradient near the interface of evaporation is low because the evaporating process is less vigorous. Moreover, a bubble transitioning from the liquid to the vapor phase can cause agitation that decreases the effect of the mass diffusion [24]. The mixture has lower heat transfer coefficient than that of pure component due to the presence of local vapor of lower boiling component in the mixture [25]. Therefore, the ethanol is having higher heat transfer coefficient and lower departure diameter than that of mixture with 75% ethanol volume fraction as shown in Figure 8. The mixture with 25% ethanol volume fraction is having highest heat transfer coefficient when compared with the other ethanol volume fractions [21, 25].

Correlation development by force balance approach

The subcooled flow boiling heat transfer coefficient is a function of $\rho, v, d_{deb}, \mu, k, f_b N_a$ and σ_s'', that is, $h = f(\mu, \rho, v_{rel}, d_h, k, f_b, N_a, \sigma_s)$. The properties and parameters chosen are combined as dimensionless numbers by Buckingham's π-theorem. These dimensionless numbers are:

$$\pi_1 = \frac{\sigma_s}{\rho v_{rel}^2 d_{dep}},$$

$$\pi_2 = \frac{d_{dep} f_b}{v_{rel}},$$
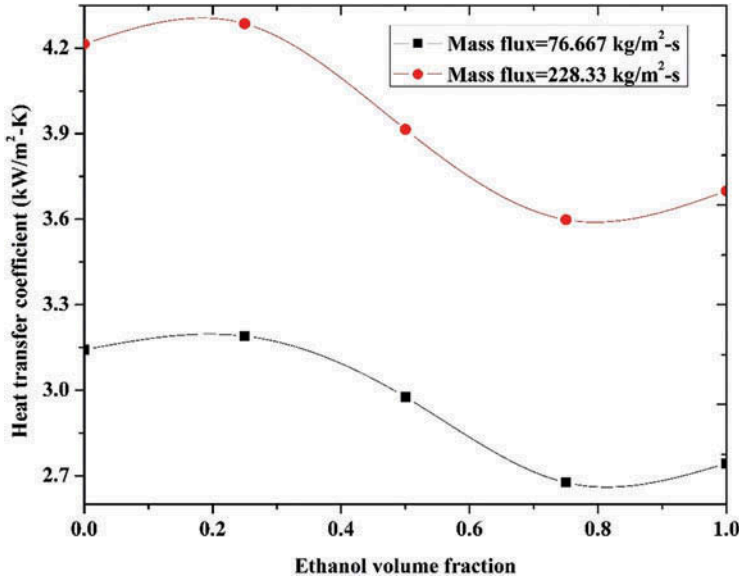
$$\pi_3 = N_a d_{dep}^2$$

and

Figure 8. Variation of subcooled flow boiling heat transfer coefficient of water ethanol mixture with ethanol volume concentration.

$$\pi_4 = \frac{hd_{dep}}{k},$$

The bubble frequency f is calculated by measured values of bubble growth period (t_g) and bubble waiting period (t_w) as shown in Eq. (19). The time period from bubble nucleation to departure is called bubble growth period. The time period from the bubble departure to the next bubble nucleation is called bubble waiting period.

$$f_b = \frac{1}{t_{wp} + t_{gp}} \tag{19}$$

$$N_a = 0.34 \times 10^4 (1 - cos\theta)\Delta T_W^2 \Delta T_{ONB} < \Delta T_w < 15K \tag{20}$$

$$N_a = 0.34 \times 10^4 (1 - cos\theta)\Delta T_W^{5.3} 15K < \Delta T_w \tag{21}$$

These dimensionless numbers can be expressed as $\pi_4 = f(\pi_1, \pi_2, \pi_3)$. The independent dimensionless numbers (π_1, π_2 and π_3) which significantly influence the dependent dimensionless number (π_4) are chosen for developing the correlation. Figures 9 to 11 show the variation of π_4 due to addition of independent dimensionless numbers. MAE is 99.6% for π_4 vs. π_1. MAE is 17.14% for π_4 vs. $\pi_1\pi_2$, 6.66% for π_4 vs. $\pi_1\pi_2\pi_3$.

$\pi_2 = \frac{d_{dep}f_b}{v_{rel}}$ and $\pi_3 = N_a d_{dep}^2$ are key factors as they reduce MAE. This shows that the bubble departure diameter and bubble frequency are the dominating factors in the present correlation. Equation (22) is obtained after the regression analysis. Equation (24) represents the final form of the correlation.

$$\frac{hd_{dep}}{k} = 87.48 \left(\frac{\sigma_s}{\rho v_{rel}^2 d_{dep}}\right)^{0.0225} \left(\frac{d_{deb}f_b}{v_{rel}}\right)^{0.044} \left(N_a d_{dep}^2\right)^{0.0048} \tag{22}$$
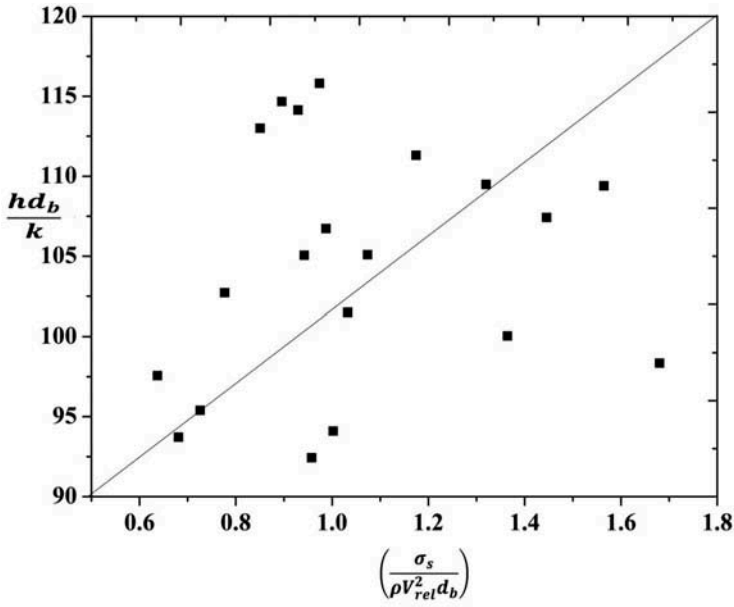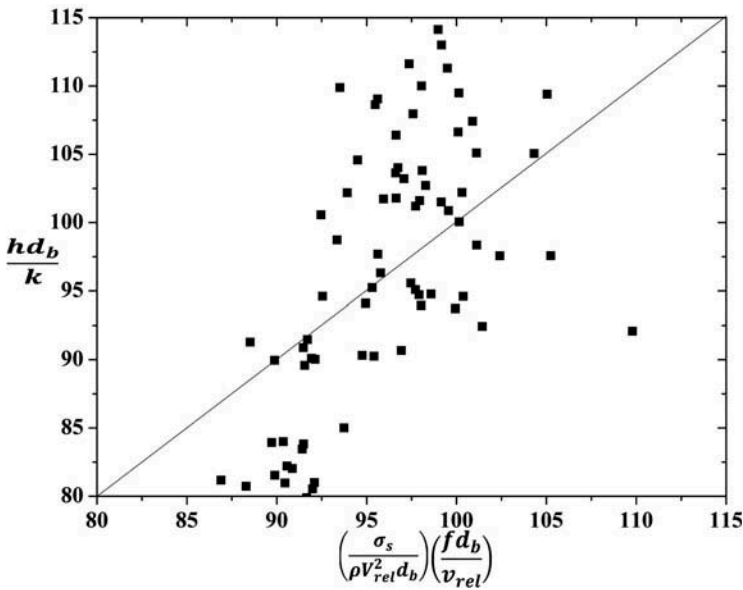
Figure 9. π_4 vs. π_1.

Figure 10. π_4 vs. $\pi_1\pi_2$.

$$Nu_{sub} = 87.48\left(\frac{1}{We_{dep}}\right)^{0.0225}(St_{rl})^{0.044}\left(N_a^*\right)^{0.0048} \tag{23}$$

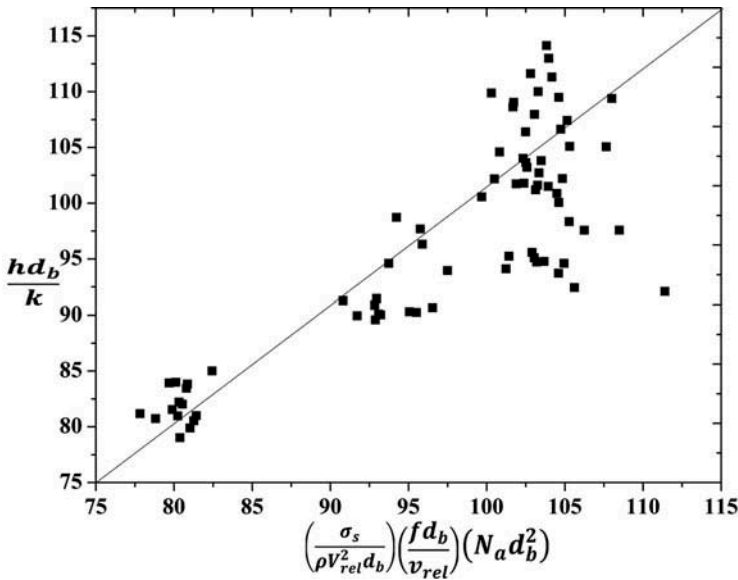$$Nu_{sub} = 87.48\frac{St_{rl}^{0.044}Na^{*0.0048}}{We_{dep}^{0.0225}} \tag{24}$$

Figure 11. π_4 vs. $\pi_1\pi_2\pi_3$.

Significance of dimensionless numbers

Bubble strouhal number

$\pi_2 = \frac{d_{dep}f_b}{v_{rel}}$ is termed as bubble strouhal number. The heat transfer coefficient decreases with increase in bubble departure diameter. In contrary, the departure diameter is in the numerator. The decrease in bubble departure is dominated by increase in bubble frequency. Heat transfer coefficient increases with increase in bubble frequency. Bubble frequency increases due to decrease in the bubble waiting period as well as bubble growth period. Increase in bubble departure diameter reduces the bubble velocity due to resistance offered by the bubble inertia to the flow. Thus, these phenomena significantly affect the heat transfer process. The large strouhal number at higher volume fraction leads to oscillatory instability. In the mixture, ethanol which is the higher volatile component evaporates earlier. Bubble formed due to evaporation of this volatile component compresses the surrounding liquid while growing and then leaves the wall surface. The incoming flow is driven to the compressible volume from the bubble which has departed. The inertia of the flow from the compressible volume will cause reduction in local pressure at the inlet of the channel which is heated. This causes to and fro motion in the channel surface leading to the compression of vapor boundary layer. The rarefaction wave also passes through the surface, thus expanding and decreasing the thermal boundary layer.

Dimensionless nucleation site density

$\pi_3 = N_a d_{dep}^2$ is dimensionless nucleation site density. The pre-existing gas nuclei in the sites cause heterogeneous nucleation. The volume of air trapped in a cavity depends on the magnitude of surface tension, contact angle, shape of the cavity, and the experimental conditions, such as system pressure, liquid temperature, and temperature of the heated surface. The wall temperature at which nucleate boiling begins depends on the availability of cavities with trapped gases. Thus, as cavities become fewer and fewer and their size decreases, the nucleation temperatures will approach homogeneous nucleation temperature [26]. Degassing removes the trapped gases in the liquid, and it is assumed that there are no pre-existing trapped gases in the liquid. The nucleation site density is assumed to be homogenous in the present study. The forced convective heat flux, evaporative heat

flux and agitation heat flux cause the phase change of the liquid in the sites causing homogeneous nucleation. The agitation heat flux is usually present in the onset of vapor generation (OSV) region of fully developed nucleate boiling regime during the subcooled flow boiling. The phase change causes the bubble generation, and these two phenomena affect the heat transfer in the liquid and the departed bubble acts as an energy carrier. The early bubble departure decreases the size of the bubble and moves away quickly. This is observed at higher heat flux and mass flux. But at higher mass flux, the bubble departs at earlier stage, and active nucleation site formation is reduced due to decrease in wall temperature. Hence, the effect of increase in heat flux on heat transfer coefficient is more significant when compared with that of mass flux. Hence, the product of the Activation nucleation site density and the bubble departure diameter is the significant parameters for heat transfer.

Comparison of force balance approach with heat transfer approach

The correlation developed using force balance approach is compared with the correlation developed using heat transfer approach as shown in Figure 12. The steps followed to develop the correlation based on heat transfer approach are given by Suhas and Sathyabhama [21]. The expression for the subcooled boiling Nusselt number developed on the basis of heat transfer approach is given by Eq. (25).

$$Nu_{scb} = 3.211 \frac{Bo^{0.048}}{We_{ch}^{0.105} Er_{tp}^{0.407}} \tag{25}$$

It is observed that 64.47% of predicted data lies within $\pm 10\%$ error when compared with those predicted using heat transfer approach correlation. The MAE of Nusselt number for water predicted using the force balance correlation and those predicted with heat transfer approach is 9.68%. The Nusselt number of water calculated from the experiment and those predicted from the force balance approach correlation as shown in Figure 13. It is found that 58.43% of predicted data lies within $\pm 10\%$ error when compared with those predicted with experimental data. The MAE of Nusselt number for water predicted using the force balance correlation and those predicted with experimental data is 9.17%. The MAE of Nusselt number of water calculated from the experiment and
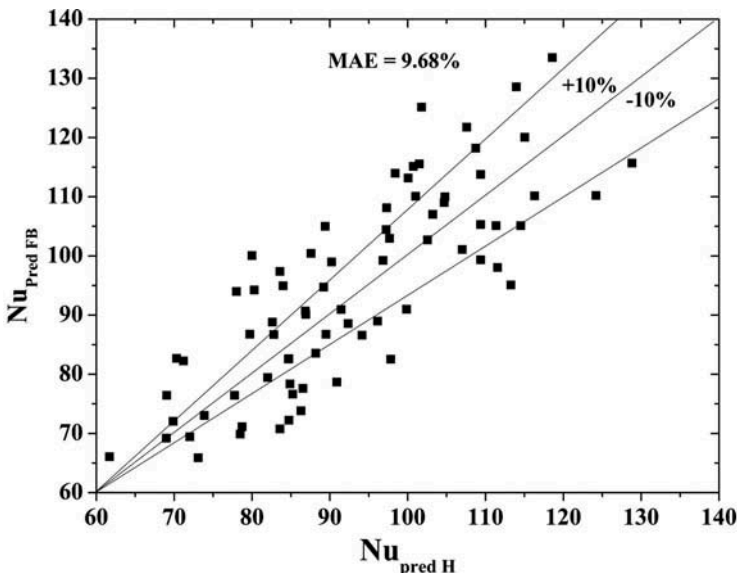

Figure 12. Validation of correlation based on heat transfer approach with the correlation based on force balance approach.
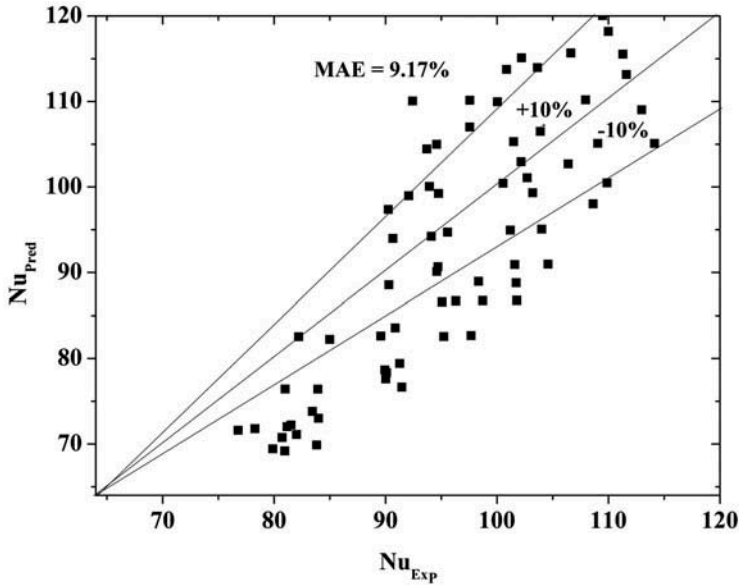
Figure 13. Validation of correlation based on force balance approach with the experimental data.
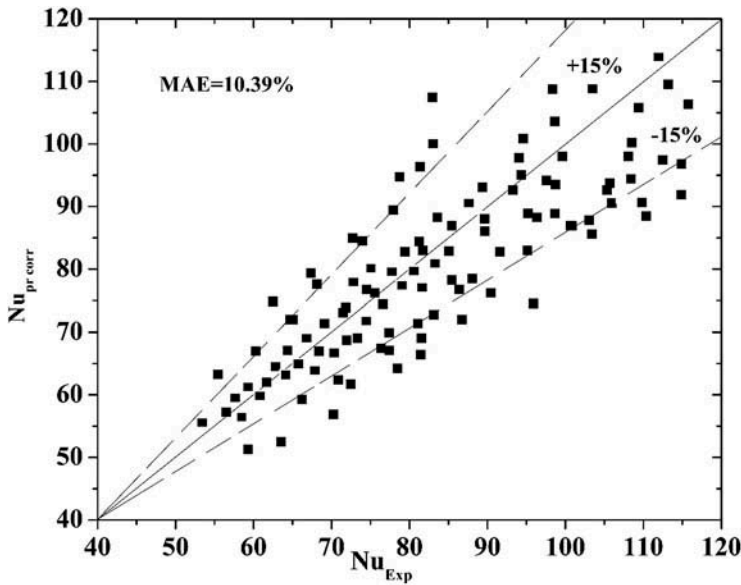

Figure 14. Validation of correlation based on heat transfer approach with the experimental data.

those predicted from the heat transfer approach correlation is 10.39% as shown in Figure 14. It is observed that 71.69% of experimental data lies within error band of $\pm 15\%$ and 37.08% of experimental data lies within error band of $\pm 10\%$. It can be seen that the force balance approach predicts the heat transfer coefficient with better accuracy when compared with heat transfer approach. The better accuracy can be attributed due to the following reasons:

The heat flux increases with increase in wall superheat at single phase forced convection and subcooled boiling region. But the increase in heat flux is higher at subcooled boiling region. The

boiling curves closely merge into a single curve for different values of mass fluxes. During the commencement of ONB, bubbly flow occurs. In bubbly flow, the liquid micro-layer film is formed due to evaporation. The bubbly flow also continues in highly subcooled OSV region. The microlayer acts as blanket and thus preventing the decrease in wall temperature. The increase in mass flux decreases the wall temperature in single phase forced convection region, but the wall superheat does not vary significantly due to increase in mass flux at subcooled boiling regions. As the mass flux increases, the wall temperature decreases due to i) diffusion of the bubbles which departed from corners and ii) formation of lesser activated nucleation sites at the bottom wall of the channel. Decrease in wall temperature decreases the wall superheat. This shows that increase in mass flux has negligible influence on heat transfer in this region. During the onset of nucleate boiling (ONB), the bubble formation commences. The active nucleation sites occur due to microlayer evaporation in the corner of bottom wall of the channel. However, flow in the middle portion of the channel is subcooled. Higher mass flux contributes toward convective mode of heat transfer, but the convective heat transfer is dominated by vapor turbulence in the flow. The bubble is subjected to variation of surface tension force, causing the bubble to depart from the surface and thus drags the adjacent warm layer of fluid. This causes local vapor momentum forces acting in the flow. These local vapor momentum forces dominate the convective mode of heat transfer to increase the heat transfer coefficient.

At higher heat flux, the buoyancy and inertial forces are significant than surface tension forces. The bubbles detach and depart from the corner and enter the subcooled region. With further increase in heat flux, the vapor generation commences, that is, onset of vapor generation (OSV). This region is highly subcooled region. This results in the increase in activated nucleation sites and also flow of surrounding fluid into the nucleation sites, when the bubbles depart from the surface. The higher heat flux also leads to earlier departure of the bubbles from the sites, thus increasing the bubble frequency. The increase in bubble frequency is due to decrease in waiting period and growth period of the bubbles. This causes vapor turbulence and agitation, which causes the heat flux contribution toward the subcooled boiling heat transfer and significant over the forced convective heat transfer. Therefore, the heat transfer coefficient increases with increase in heat flux and mass flux, but increase in mass flux is insignificant to increase the subcooled flow boiling heat transfer coefficient as shown in Figure 15. This trend is observed for all ethanol volume fractions.
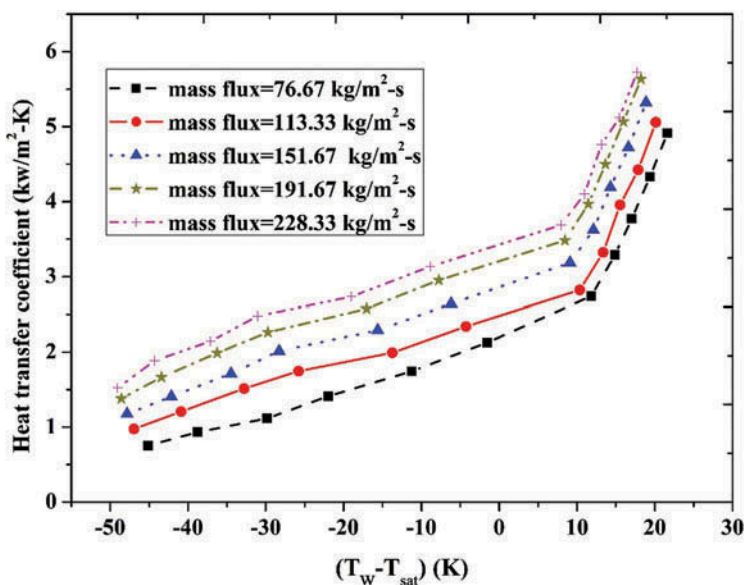

Figure 15. Variation of heat transfer coefficient of water with wall super heat.

From the above explained phenomena, it can be concluded that the nucleation sites, bubble frequency and bubble departure diameter play major role in heat transfer. Hence, by including the nucleation sites and bubble departure diameter in the force balance correlation, the heat transfer coefficient values predict the experimental values with better accuracy when compared with the heat transfer approach.

Conclusions

Bubble dynamics in water ethanol mixture subcooled flow boiling is investigated through visualization using a high speed camera for various experimental parameters like heat flux, mass flux, fluid inlet temperature and ethanol volume fraction. The heat transfer coefficient of water–ethanol mixtures is determined. Correlations are developed for subcooled flow boiling Nusselt number of water–ethanol mixture based on force balance approach. Following are the conclusions drawn from the present experiment.

- The Gungour–Winterton and Kandlikar correlations predicted the experimental data better when compared with Chen and Liu-Winterton correlations. This is attributed to the presence of dimensionless number called boiling number in the Gungour-Winterton and Kandlikar correlations.
- It is found that $\pi_2 = \frac{d_{deb}f}{v_{rel}}$ and $\pi_3 = N_a d_{deb}^2$ of force balance approach correlations are key factors as they reduce MAE.
- It is observed that the force balance approach predicts the experimental data with better accuracy when compared with that of heat transfer approach.
- Subcooled flow boiling heat transfer coefficient increases with an increase in heat flux and mass flux. But increase in mass flux is insignificant to increase the subcooled flow boiling heat transfer coefficient.

Nomenclature

Bo	Boiling number
Cp	Specific heat (kJ/kg-K)
D	Bubble diameter (mm)
D_h	Hydraulic diameter (m)
E	Enhancement factor
Exp	Experimental
f_b	Bubble frequency (s^{-1})
G	Mass flux (kg/m^2-s)
h	Heat transfer coefficient (kW/m^2-K)
h_{fg}	Latent heat of vaporization (kJ/kg)
k	Thermal conductivity (kW/m-K)
M	Molecular mass (kg/mol)
Nu	Nusselt number
N_a	Nucleation site density (sites/m^2)
ONB	Onset of Nucleate boing
OSV	Onset of vapor generation
P	Pressure (N/m^2)
Pr	Prandtl number
q"	Heat flux (kW/m^2)
Re	Reynolds number
St_{rl}	Strouhal number
V	Velocity (ms^{-1})
We	Weber number
t	Time
T	Temperature (K)
ΔT_w	Wall super heat (K)
X	Location of thermocouple

Subscripts

Cr	Critical
dep	Departure
fc	Forced convection
fr	First row
g	Vapor phase
gp	Growth period
in	Channel Inlet
l	Liquid phase
Pred	Predicted
Pred FB	Predicted values based on force balance
Pred H	Predicted values based on heat transfer approach
Pb	Pool boiling
rel	Relative motion between the bubble and the fluid flow
Sat	Saturated
sr	Second row
sub	Subcooled
tp	Two phase

Greek letters

α	Thermal diffusivity (m^2/s)
ρ	Density (kg/m^3)
μ	Dynamic viscosity (kg/m-s)
σ	Surface Tension (N/m)
θ	Contact angle (deg)

References

[1] S. M. Peyghambarzadeh, M. Jamialahmadi, S. A. Alavi Fazel, and S. Azizi. Saturated Nucleate Boiling to Binary and Ternary Mixtures on Horizontal Cylinder, *Exp. Thermal Fluid Sci.*, vol. 33, pp. 903–911, 2009.

[2] S. G. Kandlikar. Boiling Heat Transfer with Binary Mixture: Part-I, A Theoretical Modeling for Pool Boiling, *J. Heat Transfer, ASME*, vol. 120, pp. 380–387, 1998.

[3] A. Kouidri, B. Madani, and B. Roubi. Experimental Investigation of Flow Boiling in Narrow Channel, Int. *J. Thermal Sci.*, vol. 98, pp. 90–98, 2015.

[4] M. M. Mahmouda and T. G. Karayiannis. Heat Transfer Correlation for Flow Boiling in Small to Micro Tubes, Int. *J. Heat Mass. Transfer*, vol. 66, pp. 553–574, 2013.

[5] S. G. Kandlikar. Heat Transfer Mechanisms during Flow Boiling in Microchannels, *J. Heat Transfer, ASME*, vol. 126, pp. 8–16, 2004.

[6] M. C. Paz, M. Conde, E. Suarez, and M. Concheiro. On the Effect of Surface Roughness and Material on the Subcooled Flow Boiling of Water, *Exp. Thermal Fluid Sci.*, vol. 64, pp. 114–124, 2015.

[7] V. K. Dhir and G. R. Warrier. Heat Transfer and Wall Heat Flux Partitioning during Subcooled Flow Nucleate Boiling—A Review, *J. Heat Transfer*, vol. 128, pp. 1243–1256, 2006.

[8] P. K. Sarma, V. Srinivas, K. V. Sharmab, T. Subrahmanyam, and S. Kakac. A Correlation to Predict Heat Transfer Coefficient in Nucleate Boiling on Cylindrical Heating Elements, *Int. J. Thermal Sci.*, vol. 47, pp. 347–354, 2008.

[9] K. Stephan and M. Abdelsalam. Heat-Transfer Correlations for Natural Convection Boiling, Int. *J. Heat Mass. Transfer*, vol. 23, pp. 73–87, 1978.

[10] K. E. Gungor and R. H. S. Winterton. A General Correlation for Flow Boiling in Tubes and Annuli. I, *Hear Mass Transferm*, vol. 29, no. 3, pp. 351–358, 1991.

[11] L. Yin, L. Jia, and X. Mingchen. Experimental Investigation on Bubble Sliding during Subcooled Flow Boiling in Microchannel, *Exp. Thermal Fluid Sci.*, vol. 68, pp. 435–441, 2015.

[12] J. Anthony and Y. K. Li. Design Optimization of Electric Vehicle Battery Cooling Plates for Thermal Performance, *J. Power Sour.*, vol. 196, pp. 10359–10368, 2011.

[13] B. G. Suhas and Sathyabhama. Numerical Analyses of Single-Phase Pressure Drop and Forced Convective Heat Transfer Coefficient of Water–Ethanol Mixture: An Application in Cooling of HEV Battery Module, *Heat Transfer Asian Res.*, vol. 45, no. 7, pp. 680–698, 2016.

[14] B. G. Suhas and A. Sathyabhama. Bubble Dynamics of Water-Ethanol Mixture during Subcooled Flow Boiling in a Conventional Channel, *Appl. Thermal Eng.*, vol. 113, pp. 1596–1609, 2017. DOI:10.1016/j.applthermaleng.2016.11.126

[15] M. H. Kim, H. C. Lee, B. D. Oh, and S. W. Bae. Single Bubble Growth in Saturated Pool Boiling on a Constant Wall Temperature Surface, *Int. J. Multiphase Flow.*, 29, pp. 1857–1874, 2003.

[16] S. J. Kline and F. A. McClintock. "Describing Uncertainties in Single-Sample Experiments, *Mech. Eng.*, vol. 75, pp. 3–8, 1953.

[17] J. C. Chen. A Correlation for Boiling Heat Transfer to Saturated Fluids in Convective Flow, *ASME Publ.*, vol. 63, no. 2–6, pp. HT–34, 1963.

[18] W. Chen and X. Fang. A Note on the Chen Correlation of Saturated Flow Boiling Heat Transfer, *J. Refriger.*, vol. 48, pp. 100–104, 2014.

[19] Z. Liu and R. H. S. Winterton. A General Correlation for Saturated and Subcooled Flow Boiling in Tubes and Annuli, Based on A Nucleate Pool Boiling Equation, Int. *J. Heat Mass Transf.*, vol. 34, pp. 2759–2766, 1991.

[20] S. G. Kandlikar. Heat Transfer Characteristics in Partial Boiling, Fully Developed Boiling, *J. Heat Transfer.*, vol. 120, pp. 395–401, 1998.

[21] B. G. Suhas and A. Sathyabhama. Experimental Investigation of Heat Transfer Coefficient and Correlation Development for Water-Ethanol Mixture in Conventional Channel, *J. Thermal Sci. Eng. Appl, ASME*, 2017. DOI: 10.1115/1.4036202

[22] L. Minxia, C. Dang, and E. Hihara. Flow Boiling Heat Transfer of HFO1234yf and R32 Refrigerant Mixtures in a Smooth Horizontal Tube: Part I. Experimental Investigation, *Int. J. Heat. Transfer*, vol. 55, pp. 3437–3446, 2012.

[23] L. Minxia, C. Dang, and E. Hihara. Flow Boiling Heat Transfer of HFO1234yf and R32 Refrigerant Mixtures in a Smooth Horizontal Tube: Part II. Prediction Method, *Int. J. Heat Mass Transfer*, vol. 64, pp. 91–608, 2013.

[24] S. G. Kandlikar. Boiling Heat Transfer with Binary Mixture: Part-II, A Theoretical Modeling for Pool Boiling, National Heat transfer conference, Baltimore, Maryland, August 8–12, 1998.

[25] B. R. Fu, M. S. Tsou, and C. Pan. Boiling Heat Transfer and Critical Heat Flux of Ethanol–Water Mixtures Flowing through a Diverging Microchannel with Artificial Cavities, *Int. J. Heat Mass Transfer*, vol. 55, pp. 1807–1814, 2012.

[26] S. Kandlikar, M. Shoji, and V. Dhir. *Handbook of Phase Change: Boiling and Condensation, Nucleate Boiling*, Taylor and Francis, Philadelphia, PA, chap. 4, pp. 71–116.